



In-canopy sensors for state estimation of precision guided airdrop systems



Jacob Wachlin^a, Michael Ward^a, Mark Costello^{b,*}

^a Earthly Dynamics, LLC, Atlanta, GA, 30309, United States

^b Georgia Institute of Technology, Atlanta, GA, 30332, United States

ARTICLE INFO

Article history:

Received 20 February 2019

Received in revised form 18 April 2019

Accepted 18 April 2019

Available online 30 April 2019

ABSTRACT

Guided airdrop systems have traditionally used position and velocity information from a GPS receiver as their only source of feedback. The use of additional sensors in the guidance units is challenging because sensors in the guidance unit are in close proximity to powerful electric motors. Furthermore, there is a large amount of relative motion between the guidance unit and the parachute as they are coupled by a flexible network of rigging lines. By placing sensors in the parachute itself, it is possible to obtain accurate estimates of the canopy motion and orientation with low-cost sensors requiring minimal calibration. Specialized in-canopy sensor pods were developed to provide distributed sensing throughout a parachute canopy and a sensor fusion algorithm was developed to combine the raw data from these sensor pods into useful canopy state estimates. The effectiveness of this approach is demonstrated first in simulation, and then with flight test results on full-scale airdrop systems. The rich feedback signal available from in-canopy sensors can provide improved datasets for more detailed system identification as well as enabling novel guidance, navigation and control approaches which will lead directly to improved landing accuracy.

© 2019 Elsevier Masson SAS. All rights reserved.

1. Introduction

Gliding parachutes represent a simple type of aircraft to control in the sense that the canopy will quickly stabilize to a unique lateral and longitudinal trim point with a fixed control input. This means that lateral control can be achieved by simply controlling heading. Longitudinal control is not necessary but can be achieved by controlling airspeed if desired. The challenge in the control problem is that heading angle and airspeed are not typically directly measured on a guided airdrop system. Traditionally, precision guided parafoil systems have used GPS as their only feedback signal. From the position and velocity information provided by the GPS receiver, a navigation filter must be used to estimate critical states such as heading, airspeed and wind velocity.

The autonomous guidance unit (AGU) for an airdrop system is placed at the base of the rigging lines. The guidance unit consists of all of the sensing, actuation, and computation components in a compact enclosure. This creates a number of challenges for providing useful feedback. The compact AGU implies that any sensors will be in close proximity to powerful electric motors used to steer the parachute. Guided airdrop systems have been developed which

incorporated additional sensors beyond a single GPS receiver into the guidance unit [1–3]. Carter et al., for instance, described early efforts to obtain heading with a dual antenna GPS receiver, which was successful but prohibitively expensive [3]. They describe and present results for a guided airdrop system which used a single-antenna GPS coupled with inertial sensors, and magnetometer data was not used due to the electromagnetic interference problems.

Even if a solution is developed which provides extremely accurate heading information of the guidance unit, the flexible network of rigging lines that connects the guidance unit to the parachute results in significant relative motion between the two. It is of course the heading of the parachute, not the guidance unit, which needs to be controlled. The problem of relative motion between the guidance unit and parachute canopy has been well studied, and efforts have been made to identify and model this motion with 7, 8, and 9 degree of freedom models to capture the relative roll, pitch, and yaw dynamics, as well as higher order models to attempt to capture relative translation [4–7].

Gorman and Slegers presented flight test results analyzing the relative motion between the payload and parachute with the use of small, wireless sensors placed in the parachute itself [8]. Slegers et al. examined the use of in-canopy sensors to provide accurate estimates of canopy motion on a full-scale airdrop system [9]. This strategy allows direct feedback of actual canopy motion and completely bypasses the relative motion issue. Furthermore, the

* Corresponding author.

E-mail address: mark.costello@ae.gatech.edu (M. Costello).

Nomenclature

T_{IB}	rotation matrix from inertial reference frame to body reference frame	F_W	weight force
T_{S_i}	rotation matrix from body reference frame to sensor i reference frame	b	canopy span
$\vec{r}_{CG \rightarrow S_i}$	vector from body center of mass to sensor i location	\bar{c}	canopy main chord
x, y, z	position in inertial reference frame	α	angle of attack
ϕ, θ, ψ	roll, pitch, and yaw angles	β	sideslip angle
$\dot{x}, \dot{y}, \dot{z}$	velocity in inertial reference frame	b	canopy span
p, q, r	rotational velocity in body reference frame	ρ	air density
m	system mass	A, B, C	apparent mass coefficients
I_T	system inertia tensor	P, Q, R	apparent inertia coefficients
F_A, M_A	canopy aerodynamic force and moment	AGU	autonomous guidance unit
F_{AM}, M_{AM}	canopy apparent mass force and moment	ICSP	in-canopy sensor pod
F_S	payload aerodynamic force	TRW	total rigged weight
		GPS	global positioning system
		GNC	guidance, navigation, and control

parachute canopy is an ideal environment for the use of a magnetometer. Burdette, Costello, and Scheuermann presented simulation results for a strategy of fusing data from multiple, low-cost inertial sensors and GPS receivers distributed throughout a parachute canopy to provide real-time estimates of canopy motion which can be used as a feedback signal for autonomous control [10]. This approach relies on small, in-canopy sensor pods (ICSPs) consisting of accelerometer, gyroscope, magnetometer, barometer, and GPS sensors which can be mounted within the canopies of a variety of airdrop systems. Each pod has a low-power wireless radio for transmitting raw sensor data to a central processing unit mounted within the AGU, where state estimation is performed. Using the data from these pods, robust state estimation can be performed to estimate position, velocity, orientation, and rotation rates of the canopy itself. All sensors within the sensor pod package are low-cost and commercial grade, however the use of multiple sensors coupled with a sensor fusion algorithm can provide accurate system state estimates without the need for expensive and bulky tactical grade sensors.

The current work presents simulation and flight test results of the use of ICSPs to provide feedback of the canopy motion. First, a description of the ICSP hardware is provided. Next, the estimation algorithm used to fuse raw sensor data from multiple ICSPs into a useful estimate of canopy motion and orientation is presented. A strategy for modifying a typical navigation filter used for in-flight wind speed and heading estimation to incorporate feedback of the canopy heading angle is then provided. Simulation results are used to demonstrate the accuracy of the sensor fusion algorithm in identifying the “true” canopy states based on multiple sources of synthetic sensor data with realistic noise models. Finally, flight test results from two different types of full-scale airdrop systems are provided, demonstrating the ability of the ICSPs to provide greatly enhanced real-time feedback and improved understanding of canopy motion.

2. Hardware

2.1. In-canopy sensors

The in-canopy sensor pod (ICSP) consists of a wireless radio module with integrated microcontroller, a 9-axis MEMS IMU/magnetometer (3-axis accelerometer, 3-axis gyroscope, and 3-axis magnetometer), barometer, and a GPS module (see Fig. 1). Data from all sensors except the barometer are used for canopy state estimation. The barometer is not used since the sensors are inside the pressurized canopy. A lithium-polymer battery powers the pod. A micro-USB connection allows the device to be charged, and configuration parameters to be changed without re-flashing firmware.

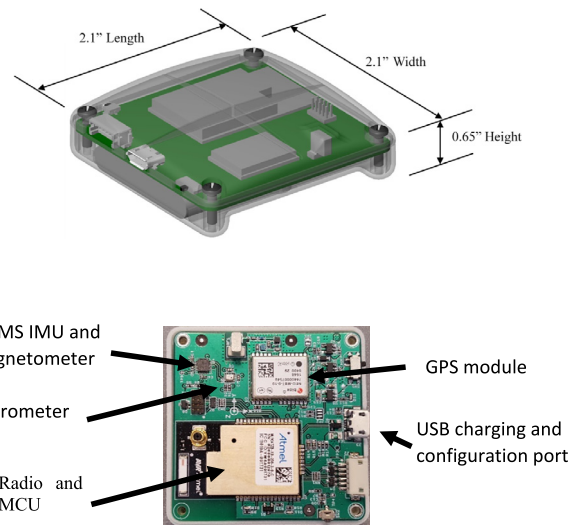


Fig. 1. Wireless in-canopy sensor pod (ICSP).

The microcontroller in the ICSP reads sensor data, provides some data filtering, applies calibration corrections, and transmits sensor data to the interface board. Accelerometer and gyroscope data are measured at 100 Hz, then filtered with a moving average filter. Data for the IMU, magnetometer, and barometer is transmitted at 10 Hz, while GPS data is received and transmitted at 5 Hz.

2.2. Interface board

For ease of integration into an AGU, hardware was developed to interface between the AGU and the wireless network. This board has two wireless radios, a microcontroller capable of performing state estimation, datalogging capability, and an RS-232 serial communication connection to the AGU (see Fig. 2).

Each radio module on the interface board has its own microcontroller, allowing it to offload message parsing tasks from the main microcontroller. The main microcontroller has an ARM Cortex-M4 processor with integrated floating-point unit (FPU), running at 120 MHz. This high performance MCU is capable of managing received messages from the radios, communicating with the AGU, logging data, and performing state estimation with in-canopy sensor data simultaneously by running a Real-Time Operating System (RTOS). The integrated FPU, along with ARM's CMSIS DSP software library allows the math-intensive state estimator with in-canopy sensor data to be run in real-time, updating nominally at 15 Hz, all while requiring less than 20% of the CPU load.



Fig. 2. Interface board.

3. Estimator design

The basic design of this estimator was developed by Burdette, Costello, and Scheuermann, but has been modified for practical implementation and to improve accuracy by using the accelerometer data, compensated by GPS measurements, to augment pitch and roll estimation [10]. The sensor network is inherently asynchronous, so the estimator was designed to be agnostic to message ordering. A no-reset distributed federated Kalman filter with local extended Kalman filters is employed [10,11]. Each ICSP is not powerful enough to perform its own state estimation, so the main MCU in the interface board runs a separate extended Kalman filter for each pod, and then fuses those results to provide a master estimate for the canopy states. Since each pod has its own filter, the local filters are completely asynchronous. Each local filter is monitored for faults such as disconnection, sensor saturation, incorrect pod installation/orientation, and stale data. The master filter is extremely robust, since it can provide state estimates even if all but one ICSP has failed, albeit with reduced accuracy.

3.1. Reference frame definitions

The inertial reference frame is a local north-east-down (NED) reference frame. The system then has a body frame of reference, with orientation of that reference frame with respect to the inertial reference frame defined using conventional aerospace Euler angles. Finally, each sensor has a reference frame corresponding to the actual sensor axes of sensitivity. The canopy geometry is assumed to be rigid once the canopy has inflated, implying that the transformation matrices between the sensor frames and the body frame are constant.

The transformation matrix between the body (B subscript) and inertial frame (I subscript), T_{IB} , is defined in terms of the body frame Euler angles as follows, where $c_x = \cos(x)$ and $s_x = \sin(x)$:

$$T_{IB} = \begin{bmatrix} c_\theta c_\psi & c_\theta s_\psi & -s_\theta \\ s_\phi s_\theta c_\psi - c_\phi s_\psi & s_\phi s_\theta s_\psi + c_\phi c_\psi & s_\phi c_\theta \\ c_\phi s_\theta c_\psi + s_\phi s_\psi & c_\phi s_\theta s_\psi - s_\phi c_\psi & c_\phi c_\theta \end{bmatrix} \quad (1)$$

$$\begin{Bmatrix} \vec{I}_B \\ \vec{J}_B \\ \vec{K}_B \end{Bmatrix} = [T_{IB}] \begin{Bmatrix} \vec{I}_I \\ \vec{J}_I \\ \vec{K}_I \end{Bmatrix} \quad (2)$$

The transformation matrices between the sensor and body reference frames, T_{S_i} , are known before flight from the canopy geometry and the orientation of the pouches in the canopy which hold the sensor pods.

$$\begin{Bmatrix} \vec{I}_{S_i} \\ \vec{J}_{S_i} \\ \vec{K}_{S_i} \end{Bmatrix} = [T_{S_i}] \begin{Bmatrix} \vec{I}_B \\ \vec{J}_B \\ \vec{K}_B \end{Bmatrix} \quad (3)$$

Finally, some vectors must be defined which consist of the offset in the body reference frame of each sensor node from the system center of mass. As with the sensor to body frame transformation matrices, these will change depending on the actual system setup and where the in-canopy sensors are installed.

$$\vec{r}_{CG \rightarrow S_i} = \Delta x_{S_i} \vec{I}_B + \Delta y_{S_i} \vec{J}_B + \Delta z_{S_i} \vec{K}_B \quad (4)$$

3.2. State and output definitions

For the implemented filter, there are 12 states per local filter (and one local filter per in-canopy sensor), 12 master filter states, and 14 output measurements. For the local filter states, the state vector is as follows:

$$X_i = [x_i, y_i, z_i, \phi_i, \theta_i, \psi_i, \dot{x}_i, \dot{y}_i, \dot{z}_i, p_{bi}, q_{bi}, r_{bi}]^T \quad (5)$$

These states are the position (x_i, y_i, z_i) in the inertial frame, the orientation of the system in Euler angles (ϕ_i, θ_i, ψ_i) the system velocity in the inertial frame ($\dot{x}_i, \dot{y}_i, \dot{z}_i$), and the individual in-canopy sensor gyroscope bias in the sensor frame (p_{bi}, q_{bi}, r_{bi}). Gyro bias in general changes over time, and therefore is estimated in real time.

For each of the local filters, a measurement vector is also defined:

$$Y_i = [x_i, y_i, z_i, \dot{x}_i, \dot{y}_i, \dot{z}_i, M_{sx_i}, M_{sy_i}, M_{sz_i}, p_{bi}, q_{bi}, r_{bi}, \phi_i, \theta_i]^T \quad (6)$$

The position and velocity measurements ($x_i, y_i, z_i, \dot{x}_i, \dot{y}_i, \dot{z}_i$) come from the GPS receiver, the magnetic field outputs ($M_{sx_i}, M_{sy_i}, M_{sz_i}$) are the magnetic field measurements in the sensor reference frame, the gyro bias outputs (p_{bi}, q_{bi}, r_{bi}) come from comparing the master filter estimated rotation with the individual sensor gyroscope measurement, and the orientation outputs (ϕ_i, θ_i) are generated from the accelerometer measurements. Yaw is not explicitly included in the measurement vector, but is implicitly included through the magnetic field measurements.

The master filter states are then defined as follows:

$$X_m = [x_m, y_m, z_m, \phi_m, \theta_m, \psi_m, \dot{x}_m, \dot{y}_m, \dot{z}_m, p_m, q_m, r_m]^T \quad (7)$$

The position, orientation, and translational velocity states ($x_m, y_m, z_m, \phi_m, \theta_m, \psi_m, \dot{x}_m, \dot{y}_m, \dot{z}_m$) are all defined in the same way as for the local state estimators, and the m subscript denotes this is the master state. The final states, rotational velocity states (p_m, q_m, r_m), are the system's rotational velocity in the system body frame. Note the master filter provides angular velocity estimates, rather than the angular velocity bias values in the local filters.

3.3. State propagation equations

The local filter state time derivatives are as follows:

$$\begin{bmatrix} \dot{x}_i \\ \dot{y}_i \\ \dot{z}_i \end{bmatrix} = \begin{bmatrix} \dot{x}_i \\ \dot{y}_i \\ \dot{z}_i \end{bmatrix} \quad (8)$$

$$\begin{bmatrix} \ddot{x}_i \\ \ddot{y}_i \\ \ddot{z}_i \end{bmatrix} = [T_{IB}]^T [T_{S_i}]^T \begin{bmatrix} a_{x_i} \\ a_{y_i} \\ a_{z_i} \end{bmatrix} + \begin{bmatrix} 0 \\ 0 \\ g \end{bmatrix} \quad (9)$$

$$\begin{bmatrix} \dot{\phi}_i \\ \dot{\theta}_i \\ \dot{\psi}_i \end{bmatrix} = \begin{bmatrix} 1 & s_{\phi_i} t_{\theta_i} & c_{\phi_i} t_{\theta_i} \\ 0 & c_{\phi_i} & -s_{\phi_i} \\ 0 & \frac{s_{\phi_i}}{c_{\theta_i}} & \frac{c_{\phi_i}}{c_{\theta_i}} \end{bmatrix} [T_{S_i}]^T \begin{bmatrix} p_i - p_{bi} \\ q_i - q_{bi} \\ r_i - r_{bi} \end{bmatrix} \quad (10)$$

$$\begin{bmatrix} \dot{p}_{bi} \\ \dot{q}_{bi} \\ \dot{r}_{bi} \end{bmatrix} = \begin{bmatrix} 0 \\ 0 \\ 0 \end{bmatrix} \quad (11)$$

These state propagation equations use accelerometer (compensated for the gravity vector) and gyroscope (compensated with the bias estimate) data to generate the state time derivatives. These equations are numerically integrated to propagate the state. The linearized dynamics are used to propagate the estimation error covariance.

3.4. Output feedback

For each sensor, a measurement signal used within the Kalman filter update step is generated. In the case of a GPS measurement, the measurement signal is directly obtained from the sensor:

$$\begin{bmatrix} x_i \\ y_i \\ z_i \end{bmatrix} = \begin{bmatrix} x_{gps} \\ y_{gps} \\ z_{gps} \end{bmatrix} \quad (12)$$

$$\begin{bmatrix} \dot{x}_i \\ \dot{y}_i \\ \dot{z}_i \end{bmatrix} = \begin{bmatrix} \dot{x}_{gps} \\ \dot{y}_{gps} \\ \dot{z}_{gps} \end{bmatrix} \quad (13)$$

For the magnetometer, the measurement in each axis of sensitivity is normalized by the total field strength before use since the calibration routine performed on the magnetometers before flight does not correct for absolute scale factors for each axis, but rather the relative scale factors between axes. It therefore can still provide information about the direction of the local magnetic field, but not necessarily accurate measurements of the field strength:

$$\begin{bmatrix} M_{sx_i} \\ M_{sy_i} \\ M_{sz_i} \end{bmatrix} = \begin{bmatrix} \frac{M_{xmag}}{\sqrt{M_{xmag}^2 + M_{ymag}^2 + M_{zmag}^2}} \\ \frac{M_{ymag}}{\sqrt{M_{xmag}^2 + M_{ymag}^2 + M_{zmag}^2}} \\ \frac{M_{zmag}}{\sqrt{M_{xmag}^2 + M_{ymag}^2 + M_{zmag}^2}} \end{bmatrix} \quad (14)$$

For the gyroscope, the “measured” bias is determined by subtracting the master estimate of the system rotation rates from the raw, measured rotation rates for that sensor:

$$\begin{bmatrix} p_{bi} \\ q_{bi} \\ r_{bi} \end{bmatrix} = \begin{bmatrix} p_i \\ q_i \\ r_i \end{bmatrix} - [T_{S_i}] \begin{bmatrix} p_m \\ q_m \\ r_m \end{bmatrix} \quad (15)$$

Finally, accelerometer measurements are used to augment pitch and roll estimation. The accelerometer measures the total acceleration in the sensor reference frame, and includes both the gravity vector and vehicle acceleration. The GPS-based compensation approach used by Kingston and Beard was used to calculate the roll and pitch [12]. The acceleration of the system in the inertial frame is calculated using a discrete derivative of the GPS velocity. This measurement, plus gravitational acceleration should be equal to the measurements from the accelerometer once rotated into the correct reference frame. These equations can be solved for the roll and pitch assuming the yaw estimate is known [12]:

$$\begin{bmatrix} a_{GPS_x} \\ a_{GPS_y} \\ a_{GPS_z} - g \end{bmatrix} = [T_{IB}]^T [T_{S_i}]^T \begin{bmatrix} a_{x_i} \\ a_{y_i} \\ a_{z_i} \end{bmatrix} \quad (16)$$

$$\begin{bmatrix} r_x \\ r_y \\ r_z \end{bmatrix} = \begin{bmatrix} \cos(\psi)a_{GPS_x} + \sin(\psi)a_{GPS_y} \\ -\sin(\psi)a_{GPS_x} + \cos(\psi)a_{GPS_y} \\ a_{GPS_z} - g \end{bmatrix} \quad (17)$$

$$\sigma_\theta = \frac{r_x a_x + r_z \sqrt{r_x^2 + r_z^2 - a_x^2}}{r_x^2 + r_z^2} \quad (18)$$

$$\theta = -\tan^{-1} \left(\frac{\sigma_\theta r_x - a_x}{\sigma_\theta r_z} \right) \quad (19)$$

$$r_\theta = r_x \sin(\theta) + r_z \cos(\theta) \quad (20)$$

$$\sigma_\phi = \frac{r_y a_y + r_\theta \sqrt{r_y^2 + r_\theta^2 - a_y^2}}{r_y^2 + r_\theta^2} \quad (21)$$

$$\phi = -\tan^{-1} \left(\frac{\sigma_\phi r_y - a_y}{\sigma_\phi r_\theta} \right) \quad (22)$$

The expected output vector \hat{Y} elements are set to their corresponding estimated values from the system state estimates, except for the magnetometer readings since those do not have a corresponding estimated value. Instead, a normalized estimate of the Earth's magnetic field is generated for the system's current location using the World Magnetic Model [13].

$$\begin{bmatrix} M_{sx_i} \\ M_{sy_i} \\ M_{sz_i} \end{bmatrix} = [T_{S_i}] [T_{IB}] \begin{bmatrix} \frac{M_{xmodel}}{\sqrt{M_{xmodel}^2 + M_{ymodel}^2 + M_{zmodel}^2}} \\ \frac{M_{ymodel}}{\sqrt{M_{xmodel}^2 + M_{ymodel}^2 + M_{zmodel}^2}} \\ \frac{M_{zmodel}}{\sqrt{M_{xmodel}^2 + M_{ymodel}^2 + M_{zmodel}^2}} \end{bmatrix} \quad (23)$$

The magnetic field vector is in the inertial reference frame, and it is transformed into the respective sensor frame using the estimated orientations to generate the transformation matrix. Note that this mapping is nonlinear, and so it is linearized to form part of the C matrix in the Kalman filtering step.

3.5. Distributed federated Kalman filter

The distributed federated Kalman filtering approach consists of carrying out the local filter operations disjoint from each other, and then combining them to generate a so-called master state estimate, which is the best estimate of the system states. Performing filtering this way versus the traditional centralized Kalman filter in which all data is processed at once is computationally more efficient and offers more robust error detection and fault handling.

There are numerous methods for performing the local filter state merging step, with varying degrees of optimality, efficiency, and robustness. The unweighted averaging method is used here.

Using unweighted averaging, the states from the N local filters are combined as an unweighted average. There is no master Kalman filter, but rather a simple merging step that combines the results from the local filters. Of course, care must be taken when averaging the orientations, due to their periodic nature:

$$\begin{bmatrix} x_m \\ y_m \\ z_m \end{bmatrix} = \frac{1}{N} \sum_{i=1}^N \left(\begin{bmatrix} x_i \\ y_i \\ z_i \end{bmatrix} - [T_{IB}]^T \vec{r}_{CG \rightarrow S_i} \right) \quad (24)$$

$$\begin{bmatrix} \phi_m \\ \theta_m \\ \psi_m \end{bmatrix} = \begin{bmatrix} \text{atan2} \left(\frac{1}{N} \sum_{i=1}^N \sin \phi_i, \frac{1}{N} \sum_{i=1}^N \cos \phi_i \right) \\ \text{atan2} \left(\frac{1}{N} \sum_{i=1}^N \sin \theta_i, \frac{1}{N} \sum_{i=1}^N \cos \theta_i \right) \\ \text{atan2} \left(\frac{1}{N} \sum_{i=1}^N \sin \psi_i, \frac{1}{N} \sum_{i=1}^N \cos \psi_i \right) \end{bmatrix} \quad (25)$$

$$\begin{bmatrix} \dot{x}_m \\ \dot{y}_m \\ \dot{z}_m \end{bmatrix} = \frac{1}{N} \sum_{i=1}^N \left(\begin{bmatrix} \dot{x}_i \\ \dot{y}_i \\ \dot{z}_i \end{bmatrix} - [T_{IB}]^T [S(\vec{\omega}_{\frac{E}{I}})] \vec{r}_{CG \rightarrow S_i} \right) \quad (26)$$

$$\begin{bmatrix} p_m \\ q_m \\ r_m \end{bmatrix} = \frac{1}{N} \sum_{i=1}^N \left([T_{S_i}]^T \begin{bmatrix} p_{gyro} - p_{bi} \\ q_{gyro} - q_{bi} \\ r_{gyro} - r_{bi} \end{bmatrix} \right) \quad (27)$$

This method is computationally efficient and allows for fairly robust error checking since the local filter results can all be compared to each other and outliers rejected. It is also extremely

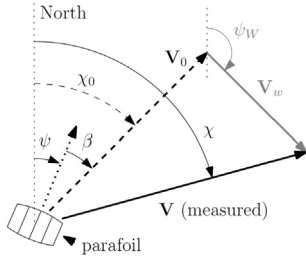


Fig. 3. Vector diagram decomposing ground track vector.

flexible, since if more sensors are added, the summation simply changes. If one sensor powers off mid-flight, the system can recognize this, and simply ignore it during the summation process.

3.6. Flight software integration

ICSP estimates can be used immediately to improve other estimates within the flight software’s navigation filter. Existing guided airdrop flight software was modified to enable the use of ICSP feedback for closed loop control of a parachute system and to augment estimation of the wind field [14]. The standard navigation problem for guided airdrop systems centers on the solution of the vector diagram in Fig. 3. The ground track velocity is measured with GPS. Airspeed can be determined from system identification techniques, accomplished either using previous flight data or in real-time. However, with only an assumed airspeed and a measurement of the ground track vector, a unique solution to the vector diagram does not exist. The solution employed for typical airdrop systems is to gather measurements over varying heading angles and solve the resulting vector diagrams simultaneously by assuming a constant wind vector. This is typically performed in real-time using an extended Kalman filter [15]. The filter is tuned based on the assumption that the wind does not change over a complete turn, and as long as there is variation in the ground course the filter will remain stable. Note that solution of the vector diagram does not directly yield an estimate of the heading angle ψ , but rather the azimuth angle χ_0 . The two are related by the sideslip angle β , which is normally assumed to be negligible for airdrop systems.

If an estimate of the heading angle can be provided using data from the ICSPs, solution of the vector diagram is greatly simplified. In fact, if the typical assumptions of known airspeed and negligible sideslip are made, the vector diagram can be solved directly and no navigation filter is required. However, these same assumptions also represent drawbacks to this approach. While a nominal value for the airspeed may be known to a fairly high degree of accuracy, there can be substantial variations in the system’s airspeed as it maneuvers or encounters turbulence. Similarly, while it should be a safe assumption that the sideslip angle is nominally zero, the system may develop significant sideslip angles as it maneuvers and encounters turbulence. Furthermore, the heading measurement provided from the ICSP state estimator is not perfect, so some noise and possibly bias from the true heading is expected.

The approach taken here is to use an extended Kalman filter similar to the one used for standard airdrop navigation. The filter is formed based on the same vector diagram, with the system heading angle and ground track vector provided as measurements. The states in the filter are the wind vector components, the filtered heading angle estimate, and error terms representing variations in true heading from the measurement and true airspeed from the assumed airspeed. The equations defining the state and measurement update equations for the filter are given in Tables 1 and 2.

Table 1
State prediction equations for navigation filter.

States	$\mathbf{x}_{p,k+1}$	=	\mathbf{f}_k	+ \mathbf{n}_k
North Wind Component (m/s)	$V_{WX,k+1}$	=	$V_{WX,k}$	+ n_{VW}
East Wind Component (m/s)	$V_{WY,k+1}$	=	$V_{WY,k}$	+ n_{VW}
Heading (rad)	ψ_{k+1}	=	ψ_k	+ n_ψ
Heading Error (rad)	$\Delta\psi_{k+1}$	=	$\Delta\psi_k$	+ $n_{\Delta\psi}$
Airspeed Error (m/s)	$V_{E,k+1}$	=	$V_{E,k}$	+ n_{VE}

Table 2
Measurement update equations for navigation filter.

Measurement	\mathbf{v}_k	=	\mathbf{g}_k	+ \mathbf{w}_k
North GPS Velocity Component (m/s)	$V_{X,k}$	=	$V_0 \cos(\psi_k) + V_{WX,k}$	+ n_{VGPS}
East GPS Velocity Component (m/s)	$V_{Y,k}$	=	$V_0 \sin(\psi_k) + V_{WY,k}$	+ n_{VGPS}
Measured Heading (rad)	$\psi_{M,k}$	=	$\psi_k + \Delta\psi_k$	+ $n_{\psi M}$

The airspeed used for the measurement update equations, V_0 , is simply the sum of the assumed nominal airspeed and the airspeed error state in the filter, V_E . These state and measurement relationships are used to develop a standard extended Kalman filter.

4. Simulation model description

A 6-DOF parafoil simulation environment was used to test the estimator against truth data, using the model described in [16]. Synthetic ICSP data with realistic error sources are generated within the model, and provided to the ICSP estimator. This simulation also features flight software with closed loop control. The flight software generates its own estimates of certain states, such as heading and heading rate, from AGU GPS data alone. The estimates from the flight software using only AGU GPS and the ICSP estimates are compared to truth data to gauge their accuracy.

4.1. System dynamics

The system states consist of the position in a North-East-Down reference frame (x, y, z), the orientation defined by Euler angles (ϕ, θ, ψ), the ground-relative body-frame velocity (u, v, w), and the ground-relative body-frame rotation rates (p, q, r):

$$\mathbf{X} = [x, y, z, \phi, \theta, \psi, u, v, w, p, q, r]^T \quad (28)$$

The kinematics equations for the system are therefore:

$$\begin{Bmatrix} \dot{x} \\ \dot{y} \\ \dot{z} \end{Bmatrix} = [T_{IB}]^T \begin{Bmatrix} u \\ v \\ w \end{Bmatrix} \quad (29)$$

$$\begin{Bmatrix} \dot{\phi} \\ \dot{\theta} \\ \dot{\psi} \end{Bmatrix} = \begin{bmatrix} 1 & s_\phi t_\theta & c_\phi t_\theta \\ 0 & c_\phi & -s_\phi \\ 0 & s_\phi / c_\theta & c_\phi / c_\theta \end{bmatrix} \begin{Bmatrix} p \\ q \\ r \end{Bmatrix} \quad (30)$$

where the matrix T_{IB} is a rotational transformation matrix from an inertial reference frame to the body reference frame.

$$T_{IB} = \begin{bmatrix} c_\theta c_\psi & c_\theta s_\psi & -s_\theta \\ s_\phi s_\theta c_\psi - c_\phi s_\psi & s_\phi s_\theta s_\psi + c_\phi c_\psi & s_\phi c_\theta \\ c_\phi s_\theta c_\psi + s_\phi s_\psi & c_\phi s_\theta s_\psi - s_\phi c_\psi & c_\phi c_\theta \end{bmatrix} \quad (31)$$

The dynamics equations are then formed as:

$$\begin{Bmatrix} \dot{u} \\ \dot{v} \\ \dot{w} \end{Bmatrix} = \frac{1}{m} \left(F_W + F_A + F_S + F_{AM} + \sum_{i=1}^N F_{BAi} \right) - S_\omega^B \begin{Bmatrix} u \\ v \\ w \end{Bmatrix} \quad (32)$$

$$\begin{Bmatrix} \dot{p} \\ \dot{q} \\ \dot{r} \end{Bmatrix} = [I_T]^{-1} \left(M_A + M_{AM} + S_{CG,P}^B F_A + S_{CG,S}^B F_S + S_{CG,M}^B F_{AM} + \sum_{i=1}^N (S_{CG,BA_i}^B F_{BA_i}) - S_{\omega}^B [I_T] \begin{Bmatrix} p \\ q \\ r \end{Bmatrix} \right) \quad (33)$$

where m is the system mass, I_T is the system inertia matrix, F_A , M_A are the aerodynamic force and moment vectors in the body reference frame, F_{AM} , M_{AM} are the apparent mass force and moment vectors in the body reference frame, F_S is the payload drag in the body reference frame, F_W is the weight vector in the body reference frame, S_{ω}^B is the cross-product matrix of angular velocity in the body reference frame, and $S_{CG,P}^B$, $S_{CG,S}^B$, $S_{CG,M}^B$ are the cross-product matrices of the vector from the center of mass to the aerodynamic center, payload, and apparent mass center, respectively. F_{BA_i} is the aerodynamic force vector caused by activation of the i th bleed air actuator, and S_{CG,BA_i}^B is the cross-product matrix of the vector from the center of mass to the location of the i th bleed air actuator [17]. The aerodynamic force and moment perturbations from bleed air actuators are summed over the N actuators in the system. The weight force is given by the following, where m is the system mass and g is the gravitational acceleration:

$$F_W = mg \begin{Bmatrix} -S_{\theta} \\ S_{\phi} C_{\theta} \\ C_{\phi} C_{\theta} \end{Bmatrix} \quad (34)$$

The aerodynamic forces are then generated as follows. First, the aerodynamic translational and rotational velocities are calculated, taking into account atmospheric wind velocity:

$$\begin{Bmatrix} u_{A,CG} \\ v_{A,CG} \\ w_{A,CG} \end{Bmatrix} = \begin{Bmatrix} u - u_{wind} \\ v - v_{wind} \\ w - w_{wind} \end{Bmatrix} \quad (35)$$

$$\begin{Bmatrix} p_{A,CG} \\ q_{A,CG} \\ r_{A,CG} \end{Bmatrix} = \begin{Bmatrix} p - p_{wind} \\ q - q_{wind} \\ r - r_{wind} \end{Bmatrix} \quad (36)$$

The payload aerodynamic loads are then formed. First the aerodynamic velocity of the payload in the body frame is found, then the forces are calculated, where ρ is the air density, S_S is the payload reference area, and C_{DS} is the payload drag coefficient:

$$\begin{Bmatrix} u_S \\ v_S \\ w_S \end{Bmatrix} = \begin{Bmatrix} u_{A,CG} \\ v_{A,CG} \\ w_{A,CG} \end{Bmatrix} + S_{\omega_{A,CG}}^B \begin{Bmatrix} \Delta x_S \\ \Delta y_S \\ \Delta z_S \end{Bmatrix} \quad (37)$$

$$V_S = \sqrt{u_S^2 + v_S^2 + w_S^2} \quad (38)$$

$$F_S = -\frac{1}{2} \rho V_S S_S C_{DS} \begin{Bmatrix} u_S \\ v_S \\ w_S \end{Bmatrix} \quad (39)$$

The canopy aerodynamics are then calculated as follows, where Γ is the canopy incidence angle, and T_{BC} is the single axis transformation matrix from body reference frame to the canopy reference frame:

$$\begin{Bmatrix} \tilde{u} \\ \tilde{v} \\ \tilde{w} \end{Bmatrix} = [T_{BC}] \left(\begin{Bmatrix} u_{A,CG} \\ v_{A,CG} \\ w_{A,CG} \end{Bmatrix} + S_{\omega}^B \begin{Bmatrix} \Delta x_c \\ \Delta y_c \\ \Delta z_c \end{Bmatrix} \right) \quad (40)$$

$$\begin{Bmatrix} \tilde{p} \\ \tilde{q} \\ \tilde{r} \end{Bmatrix} = [T_{BC}] \begin{Bmatrix} p_{A,CG} \\ q_{A,CG} \\ r_{A,CG} \end{Bmatrix} \quad (41)$$

$$T_{BC} = \begin{bmatrix} c_{\Gamma} & 0 & -s_{\Gamma} \\ 0 & 1 & 0 \\ s_{\Gamma} & 0 & c_{\Gamma} \end{bmatrix} \quad (42)$$

$$V_A = \sqrt{\tilde{u}^2 + \tilde{v}^2 + \tilde{w}^2} \quad (43)$$

$$\alpha = \text{atan} \left(\frac{\tilde{w}}{\tilde{u}} \right) \quad (44)$$

$$\beta = \text{asin} \left(\frac{\tilde{v}}{V_A} \right) \quad (45)$$

$$F_A = \frac{1}{2} \rho V_A^2 S_p \begin{Bmatrix} -\cos(\Gamma - \alpha) C_{DP} - \sin(\Gamma - \alpha) C_{LP} \\ C_{\gamma} \\ \sin(\Gamma - \alpha) C_{DP} - \cos(\Gamma - \alpha) C_{LP} \end{Bmatrix} \quad (46)$$

$$M_A = \frac{1}{2} \rho V_A^2 S_p [T_{BC}]^T \times \begin{Bmatrix} \frac{b^2}{2V_A} (C_{lp} \tilde{p} + C_{lr} \tilde{r}) + b C_{l\delta a} \delta_a \\ \frac{\bar{c}^2}{2V_A} C_{mq} \\ \frac{b^2}{2V_A} (C_{np} \tilde{p} + C_{nr} \tilde{r}) + b C_{n\beta} \beta + b C_{n\delta a} \delta_a \end{Bmatrix} \quad (47)$$

In the above equations, b is the canopy span, \bar{c} is the canopy main chord, α is the angle of attack, β is the sideslip angle, δ_a is the asymmetric control input, and C_{lp} , C_{lr} , $C_{l\delta a}$, C_{mq} , C_{np} , C_{nr} , $C_{n\beta}$, $C_{n\delta a}$ are all aerodynamic coefficients.

The bleed air actuators are each modeled as follows, in the body reference frame:

$$F_{BA_i} = \frac{1}{2} \rho V_A^2 S_{BA} \begin{Bmatrix} -C_{dBA} \delta_{BA_i} \\ 0 \\ -C_{lBA} \delta_{BA_i} \end{Bmatrix} \quad (48)$$

Here, C_{dBA} is a drag control sensitivity coefficient, C_{lBA} is a lift control sensitivity coefficient, S_{BA} is the reference area of the bleed air model, and δ_{BA_i} is the normalized line position of the actuator (actual line position divided by maximum line displacement).

Parafoils have a low mass-to-volume ratio, so apparent mass effects substantially contribute to the system dynamics. The apparent mass force and moments equations create a coupling between the rotational and translational system dynamics, so that the total system dynamics must be found as a matrix solution. Define the following, where A , B , C , P , Q , R are apparent mass and apparent inertia coefficients from the surrounding fluid that is accelerated by the canopy as it is in motion.

$$F = F_W + F_A + F_S + \sum_{i=1}^N F_{BA_i} - m S_{\omega}^B \begin{Bmatrix} u \\ v \\ w \end{Bmatrix} \quad (49)$$

$$M = M_A + S_{CG,P}^B F_A + S_{CG,S}^B F_S + \sum_{i=1}^N (S_{CG,BA_i}^B F_{BA_i}) - S_{\omega}^B [I_T] \begin{Bmatrix} p \\ q \\ r \end{Bmatrix} \quad (50)$$

$$I'_{AM} = [T_{BC}]^T \begin{bmatrix} A & 0 & 0 \\ 0 & B & 0 \\ 0 & 0 & C \end{bmatrix} [T_{BC}] \quad (51)$$

$$I'_{AI} = [T_{BC}]^T \begin{bmatrix} P & 0 & 0 \\ 0 & Q & 0 \\ 0 & 0 & R \end{bmatrix} [T_{BC}] \quad (52)$$

Then, solve the following system of equations:

$$\begin{bmatrix} m[I] + [I'_{AM}] & -[I'_{AM}]S_{CG,M}^B \\ S_{CG,M}^B [I'_{AM}] & [I_T] + [I'_{AI}] - S_{CG,M}^B [I'_{AM}] S_{CG,M}^B \end{bmatrix} \begin{Bmatrix} \dot{u} \\ \dot{v} \\ \dot{w} \\ \dot{p} \\ \dot{q} \\ \dot{r} \end{Bmatrix} = \begin{Bmatrix} F \\ M \end{Bmatrix} \quad (53)$$

4.2. Wind model

Airdrop system performance is greatly affected by wind conditions. It is therefore critical that an accurate wind model is used within the simulation environment. The wind field used in the simulation consists of the combination of an altitude-varying mean wind field and turbulence. The discrete Dryden turbulence model is used here, as described in Military Specification MIL-F-8785C [18].

4.3. Synthetic sensor data generation

This simulation has the ability to generate synthetic ICSP and AGU GPS data. All sensor data is generated at a nominal rate, with some jitter in the actual rate. Each sensor type has a noise and error model. It is assumed that the system is effectively rigid, so that rigid body kinematics apply between the system truth states and the sensors within the canopy. In addition to the noise and error models of each sensor channel, the orientation and position of the modeled sensors is perturbed from what is assumed in the estimator, to model uncertainty in those parameters.

4.3.1. GPS

The GPS sensor model provides position, velocity, and time data. The position and velocities are generated by using the truth states from the parafoil simulation and adding exponentially correlated Gaussian noise. The true value of the GPS sensor is y_k , v_k is the measured value, and n_k is the measurement noise. This data is then discretized into integer values, saturating as necessary:

$$v_k = y_k + n_k \quad (54)$$

$$n_k = e^{-\frac{\Delta t}{\tau}} n_{k-1} + \xi_k \sqrt{1 - e^{-\frac{2\Delta t}{\tau}}} \quad (55)$$

$$\xi_k \sim N(0, \sigma) \quad (56)$$

4.3.2. Accelerometer

A 3-axis accelerometer model provides the acceleration vector at a point of interest. First the truth acceleration values are generated from the simulation model, including the gravity vector. Scale factor errors and cross-axis sensitivity are applied. Then, bias values are added, modeled as a random walk process. Next, zero-mean Gaussian noise is added to each axis. Finally, the accelerometer data is discretized into 16-bit signed integer values for each axis, saturating as necessary.

4.3.3. Gyroscope

A 3-axis gyroscope model generates angular velocity vector data on a body of interest. First the truth rotational rate values are generated from the simulation model. Scale factor errors and cross-axis sensitivity are applied. Then, bias values are added, modeled as a random walk process. Next, zero-mean Gaussian noise is added to each axis. Finally, the gyroscope data is discretized into 16-bit signed integer values for each axis, saturating as necessary.

Table 3
Sensor model error parameters.

Parameter	Value	Parameter	Value
GPS horizontal velocity σ	0.2 m/s	GPS horizontal position σ	2.0 m
GPS horizontal velocity τ	1.0 s	GPS horizontal position τ	20.0 s
GPS vertical velocity σ	0.2 m/s	GPS vertical position σ	2.0 m
GPS vertical velocity τ	1.0 s	GPS vertical position τ	20.0 s
Accelerometer noise std. dev.	0.05 g	Magnetometer noise std. dev.	0.5 μ T
Gyro noise std. dev.	2.5°/s	Gyroscope initial biases	1.0°/s
Accelerometer initial biases	0.003 g	Magnetometer initial biases	1.0 μ T

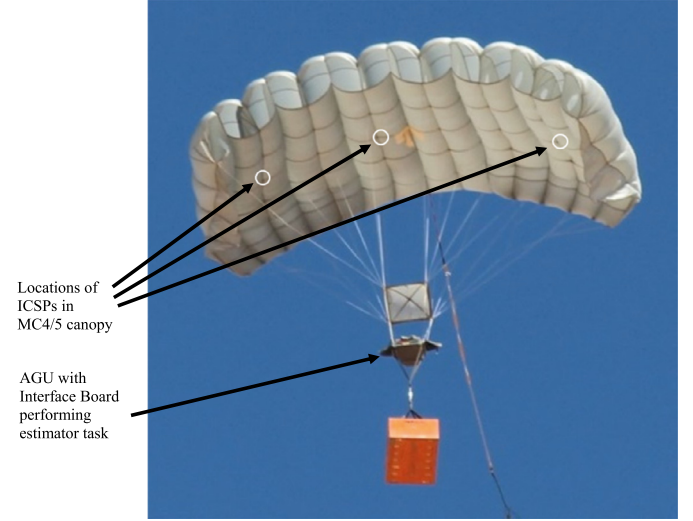


Fig. 4. Example MC5 system, canopy sensor pod mounting locations near the center and wind tips are indicated by rings.

4.3.4. Magnetometer

A 3-axis magnetometer model provides the Earth's magnetic field vector data at a point of interest. First the truth magnetic field values are generated using the World Magnetic Model. Scale factor errors and cross-axis sensitivity are applied. Then, bias values are added, modeled as a random walk process. Next, zero-mean Gaussian noise is added to each axis. Finally, the magnetometer data is discretized into 14-bit signed integer values for each axis, saturating as necessary.

5. Estimator performance

The simulation was used to test the ICSP state estimator and compare its performance to conventional methods using GPS measurements alone. The simulation uses accurate, previously validated models. Since it is a simulation, all truth states are known and can be directly compared to the generated state estimates. For this simulation, the sensor error model parameters are shown in Table 3.

5.1. MC5 system

The estimator was tested in simulation with a model of a MC5 system. The MC5 is a retired personnel ram-air parafoil with typical total weight range of 200–500 pounds. This canopy is shown in Fig. 4.

The ICSP estimator is able to accurately track heading and heading rate. Fig. 5 shows these truth states, as well as the ICSP estimate and the GPS-only estimate as the flight software performs a turn. The ICSP estimate is much closer to the truth state than the GPS-only estimate. In particular, the heading rate estimate is able to track changes with much less lag and is able to begin estimation much sooner after the start of flight.

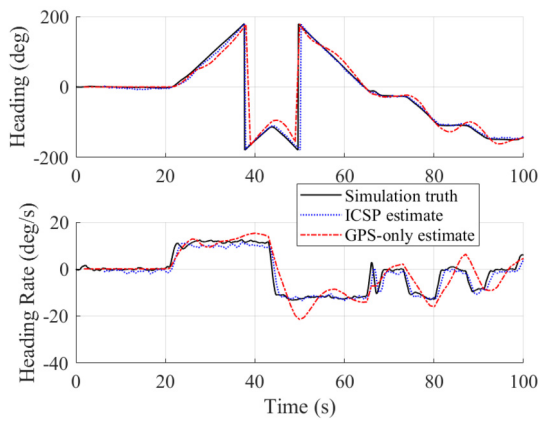


Fig. 5. Heading and heading rate truth and estimates during start of flight for simulated MC5.

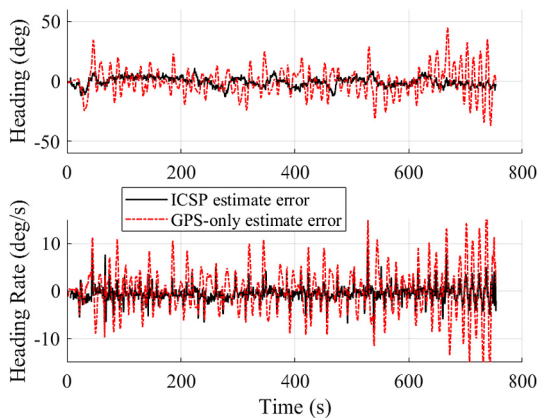


Fig. 6. Heading and heading rate estimator errors for simulated MC5 flight.

Table 4

Statistics on heading and heading rate estimate errors for simulated MC5 system.

	Mean of absolute value	Mean	Standard deviation
ICSP heading error	3.11°	−0.50°	3.81°
GPS-only heading error	8.54°	−0.36°	11.40°
ICSP heading rate error	1.30°/s	−0.68°/s	1.64°/s
GPS-only heading rate error	3.60°/s	0.04°/s	4.81°/s

Indeed, throughout the entire simulated flight, the ICSP heading and heading rate estimates are typically much better than the GPS-only estimates. Fig. 6 shows the heading and heading rate estimation errors throughout the simulated flight. The heading rate error especially is much better for the ICSP estimator. Since it uses data from the in-canopy gyroscopes, it can recognize changes in heading rate quickly, while the GPS-only estimator must observe these changes through inertial position and velocity changes; this inherently adds lag.

Table 4 provides some statistics about the accuracy of the ICSP and the GPS-only estimates of heading and heading rate for this simulated MC5 system.

Since wind field estimation is coupled with heading estimation, it is expected that the improved heading estimates from the ICSPs will lead to better wind field estimates [15]. Fig. 7 shows the truth wind field and the estimates using ICSPs and GPS-only.

The ICSP estimator provides complete orientation estimates of the system. Fig. 8 shows that these estimates track the truth states quite well.

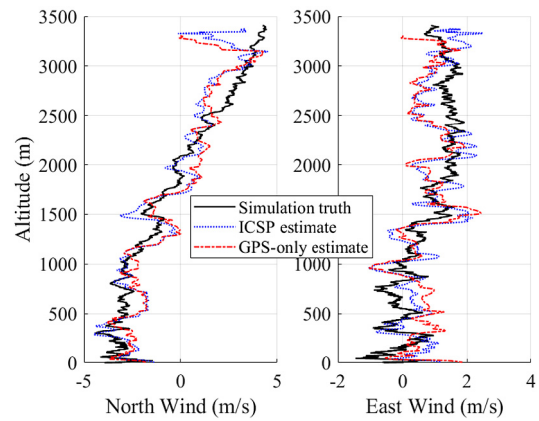


Fig. 7. Wind field truth and estimates using both the ICSP and GPS-only heading estimate within the wind field estimator for a simulated MC5.

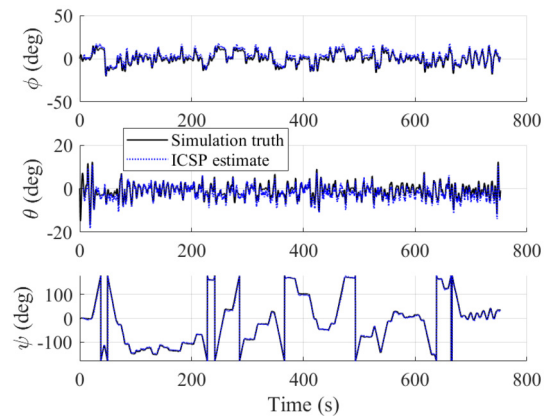


Fig. 8. Orientation estimate and truth values of a simulated MC5 system.

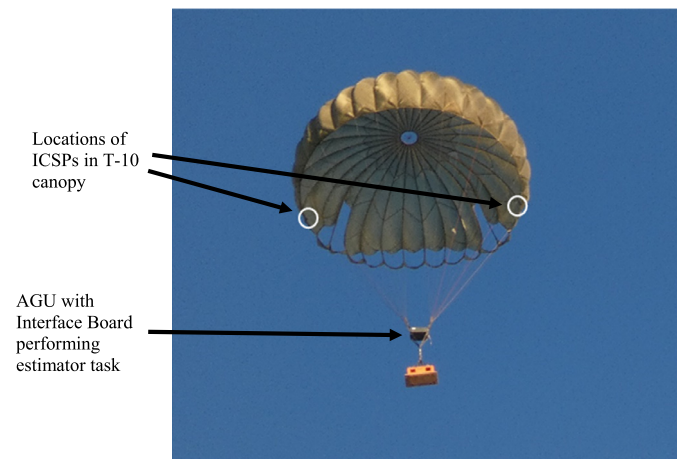


Fig. 9. Example T-10 7TU system, with the in-canopy sensor pod mounting locations on each side indicated by rings.

5.2. T-10 7TU system

The ICSP estimator was also tested using a model of a T-10 7TU system, as shown in Fig. 9. This system consists of a steerable round canopy and has a typical maximum weight range of 360 lbs. Two ICSPs are installed inside the canopy.

As it is a steerable round canopy, the T-10 7TU is a much lower horizontal airspeed system than parafoil systems of comparable capacity. This forces consecutive GPS datapoints closer together in space, and makes the task of estimating heading and heading rate

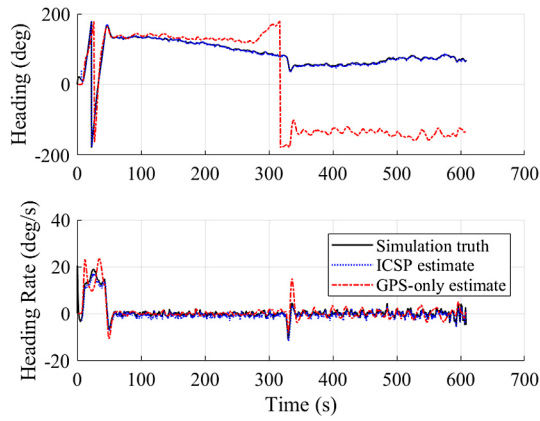


Fig. 10. Heading and heading rate truth and estimates for the simulated T-10 7TU.

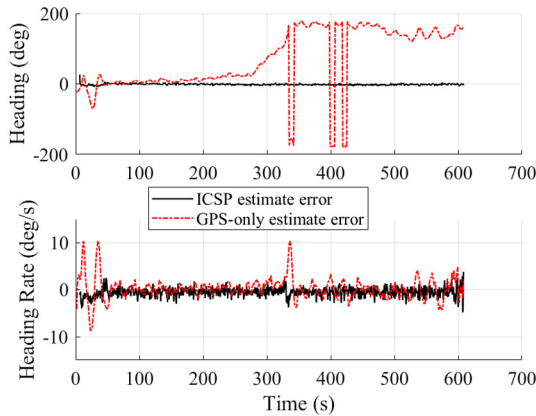


Fig. 11. Heading and heading rate estimation errors for a simulated T-10 7TU system.

Table 5
Statistics on heading and heading rate estimate errors for simulated T10 system.

	Mean of absolute value	Mean	Standard deviation
ICSP heading error	1.96°	-1.28°	2.13°
GPS-only heading error	84.93°	68.86°	85.61°
ICSP heading rate error	0.84°/s	-0.63°/s	0.85°/s
GPS-only heading rate error	1.50°/s	0.19°/s	2.3°/s

with only GPS much more difficult. This canopy can turn nearly in place, changing its heading without changing the information that GPS can provide. When this occurs, heading is unobservable to the GPS-only estimator. In addition, due to the low glide slope of the system, if it is released a significant distance from the target, a typical guidance strategy is to point at the target and glide as far as possible. This can result in a flight with nearly constant course, and so the coupled wind-field and heading estimator using GPS alone can diverge from the truth. Fig. 10 shows an example case. The system has long sections of nearly constant heading, and the ICSP estimator is able to track the truth throughout while the GPS-only estimator diverges.

Fig. 11 shows the heading and heading rate estimation errors for both the ICSP and GPS-only methods. The inverted spikes are heading wrapping between ±180 deg. Clearly, the GPS-only heading estimates quickly become useless for controlling this system. Table 5 provides statistics about these errors, showing that the ICSP estimator provides better heading and heading rate estimates than the GPS-only estimator.

Fig. 12 shows the wind field during this simulation. Since the wind field estimate is linked with the system heading estimate, the

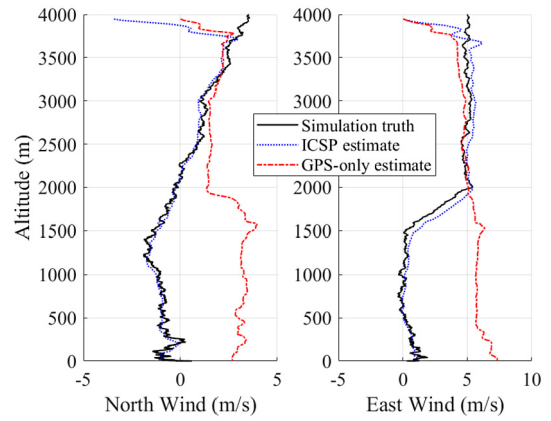


Fig. 12. Wind field truth and estimates using both the ICSP and GPS-only heading estimate within the wind field estimator for a simulated T-10 7TU.

Table 6
Statistics on wind estimate errors for simulated T10 system.

	Mean of absolute value [m/s]	Mean [m/s]	Standard deviation [m/s]
North wind error, ICSP est.	0.33	-0.21	0.83
East wind error, ICSP est.	0.44	0.19	0.70
North wind error, GPS-only est.	2.59	2.37	2.08
East wind error, GPS-only est.	3.15	2.58	3.10

system is able to recognize the wind shift much more accurately using the ICSP estimator feedback than GPS-only. The GPS-only estimator believed that the wind shift at 2000 m was due to a turn, whereas the ICSP estimator is able to recognize the change in wind and track heading correctly. Table 6 provides statistics about the wind field estimates shown in Fig. 12.

6. Flight experimentation results

To test the ICSP state estimator, it was run in real-time during flights of the two different types of airdrop systems previously simulated. Flight testing was conducted in Eloy, AZ over a one week period. The first type of system utilizes an MC5 ram-air canopy. Ram-air canopies have become the standard for guided airdrop systems. The second type of canopy is a modified T-10 round parachute, which offers lower gliding performance but also lower cost compared to a ram-air parachute.

Heading and heading rate are shown for one flight of each type of system flown with the estimator. Although the ICSP estimator provides a full state estimate of position, velocity, orientation, and rotation rates, heading and heading rate are of most interest. These states are critical to GNC, yet can be difficult to estimate using only GPS, especially in cases of significant sideslip, or minimal ground speed such as when flying into the wind.

6.1. MC5 system

The MC5 system shown in Fig. 4 typically has a total rigged weight (TRW) of between 200 and 500 lbs. Flight test results are shown for a TRW of 245 lbs. Three ICSPs are used within this canopy, one at each wingtip and one near the center. Each pod is mounted inside a pouch sewn into a rib of a cell.

Fig. 13 shows the heading and heading rate estimates for a section of an MC5 flight. The inverted spikes are heading wrapping between ±180 deg. The ICSP estimator and GPS-only estimator results are shown, as well as heading and heading rate calculated in post-processing from GPS data. The GPS data is post processed using the AGU GPS data, with a zero-lag Kalman filter. It therefore

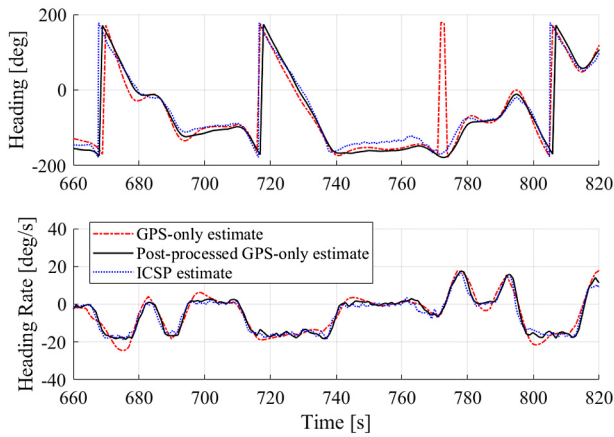


Fig. 13. Heading and heading rate estimates for a section of an MC5 system flight.

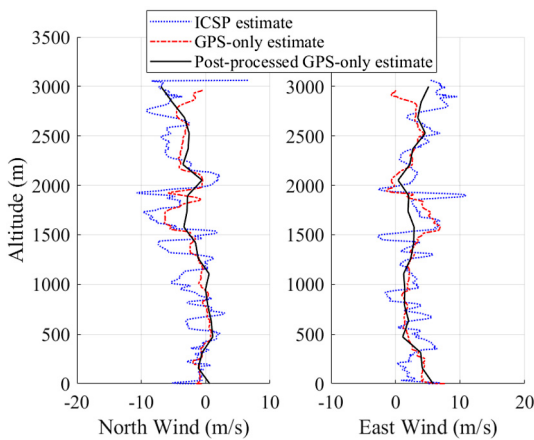


Fig. 14. Comparison of wind estimates from AGU based navigation vs. ICSP based navigation for an MC5 flight.

represents a best estimate of heading and heading rate from GPS without any delays that are inherent in a real-time estimator. This post-processing method is non-causal, so cannot be used in-flight, but represents a better reference than the in-flight GPS-only estimate. Throughout the flight, the ICSP estimates are often closer to the post-processed results than the in-flight GPS-only estimates, indicating the ICSP estimator is producing trustworthy estimates.

Fig. 14 compares the wind field estimates generated using GPS-only and using the ICSP estimates. While there is no truth signal to compare to, it is clear that estimates using the ICSP data vary much quicker. Ideally, this means the estimator is able to recognize changes in the wind field more quickly than if only GPS data were used.

Aggressive maneuvers can be unobservable, or nearly so, to the GPS-only estimator, and while they could be useful for shedding altitude under windy conditions, such maneuvers are typically avoided since they would need to be performed open-loop. On the other hand, the ICSP estimator is able to provide state estimates throughout highly acrobatic turns. During flight testing, the MC5 system was intentionally flown into a right-hand spiral. Fig. 15 shows the heading and heading rate estimates for the system throughout this maneuver.

The ICSP estimator is able to sense the right-hand turn, and continually estimate heading throughout. The heading rate estimate also is around the expected magnitude. GPS-only estimation is completely unable to perform heading or heading rate estimation throughout this spiral, and even estimates a heading rate in the wrong direction.

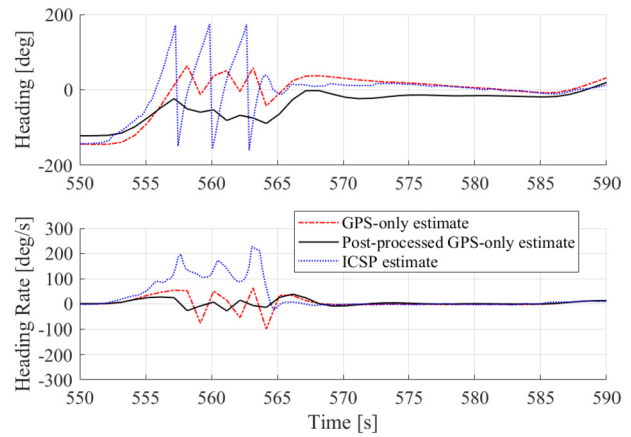


Fig. 15. Heading and heading rate estimates through a spiral on the MC5 system.

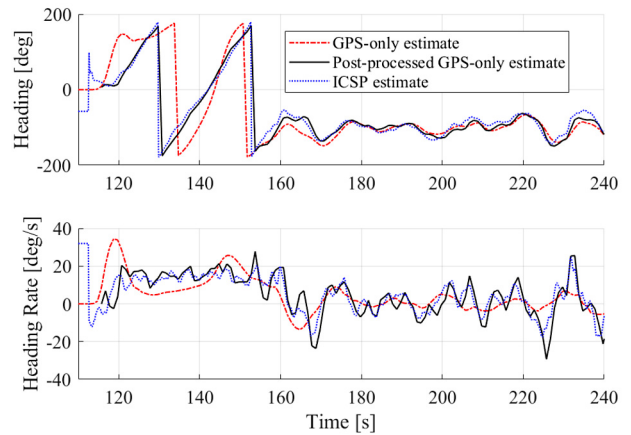


Fig. 16. Heading and heading rate estimates for a section of a T-10 7TU system flight.

6.2. T-10 7TU system

The behavior of the T-10 7TU is quite different from a ram-air gliding parachute. It can be manufactured for a much lower cost than a comparably sized ram-air parachute, but it is capable of a glide slope of about 0.6 compared to typical glide ratios of 2–3 for ram-air parachutes. This low glide ratio means that the T-10 has a much lower forward airspeed, which makes it even more difficult to separate the air-relative component of the canopy velocity from the measured ground track. Coupled with low yaw-inertia, this makes the modified T-10 a particularly difficult type of parachute to steer autonomously when using only GPS feedback from the AGU. During flight experimentation, two sensor pods were installed in the T-10 system, one on each side of the canopy. Flight test results are shown for a TRW of 252 lbs. Fig. 9 shows the setup of this system.

Fig. 16 shows the heading and heading rate estimates for a section of a T-10 7TU flight. The post-processed GPS estimate shows more oscillations in heading rate than the in-flight GPS estimate, and the oscillations tend to match well with those determined by the ICSP estimator, indicating it is providing higher fidelity feedback on the system's motion.

Finally, the performance of the updated navigation filter which is taking in the heading measurement from the in-canopy based state estimator is compared to the typical GPS based filter used on current airdrop systems. There is no true wind profile to compare to in this case, but a simple comparison between the two navigation solutions is enlightening. Fig. 17 shows the in-flight wind estimates obtained from the conventional AGU GPS based naviga-

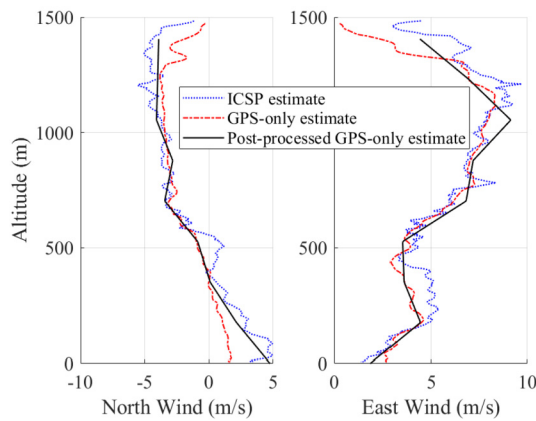


Fig. 17. Comparison of wind estimates from AGU based navigation vs. ICSP based navigation for a T-10 7TU flight.

tion filter vs. the estimates obtained from the updated filter that uses the ICSP data. The wind profiles look quite similar, but it is clear that the updated filter is tracking changes in the wind much more rapidly than the conventional GPS based filter. This promises to further enhance accuracy and robustness to variable wind conditions by providing rapid and accurate in-flight updates to the measured wind profile.

7. Conclusion

Small, low-cost, lightweight in-canopy sensor pods (ICSPs) have been developed which can be distributed throughout a parachute canopy and used to provide accurate 6-DOF canopy state estimates when combined with a robust sensor fusion and state estimation algorithm. By design, this system allows for redundancy and flexibility.

Performing state estimation using ICSPs has some advantages over the legacy approach which uses GPS only. The ICSPs are able to directly measure rotational velocity through their rate gyros, and therefore the ICSP state estimator can provide a more accurate rotation rate estimate with reduced lag. In addition, the ICSP state estimator is able to estimate heading using magnetometer data, which enables wind field estimation during straight flight. The ICSP state estimator also does not experience degraded heading and heading rate estimation performance during low groundspeed situations, such as during aggressive maneuvering of a ram-air parafoil system, high headwind conditions, or normal flight of a low-glide steerable round canopy system.

The ICSP state estimator described here was tested in simulation and experimental flight testing on ram-air parafoil (MC5) and steerable round (T-10 7TU) guided airdrop systems. In both simulation and experimental testing, the ICSP estimator performed well. In simulation, the ICSP state estimates tracked truth states closely, with minimal lag, while the equivalent states estimated through GPS alone often showed significant overshoot and phase shift.

Declaration of Competing Interest

No competing interest.

Acknowledgements

The authors would like to acknowledge the funding and flight test support of the Natick Soldier Research, Development and Engineering Center (NSRDEC) Airdrop Technology Team.

References

- [1] T.W. Bennett, R.J. Fox, Design, development flight testing of the NASA X-38 7500 ft2 parafoil recovery system, in: 17th AIAA Aerodynamic Decelerator Systems Technology Conference and Seminar, Monterey, 2003.
- [2] T. Jann, Advanced features for autonomous parafoil guidance, navigation and control, in: 18th AIAA Aerodynamic Decelerator Systems Technology Conference and Seminar, Munich, 2005.
- [3] D. Carter, S. George, P. Hattis, M. McConley, S. Rasmussen, L. Singh, Autonomous large parafoil guidance, navigation, and control system design status, in: 19th AIAA Aerodynamic Decelerator Systems Technology Conference and Seminar, Williamsburg, 2007.
- [4] N.J. Slegers, Effects of canopy-payload relative motion on control of autonomous parafoils, *J. Guid. Control Dyn.* 33 (1) (2010) 116–125.
- [5] C. Gorman, N. Slegers, Modeling of parafoil-payload relative yawing motion on autonomous parafoils, in: 21st AIAA Aerodynamic Decelerator Systems Technology Conference and Seminar, Dublin, 2011.
- [6] R. Decker, O. Yakimenko, Automated canopy and payload motion estimation using vision based methods, in: 23rd AIAA Aerodynamic Decelerator Systems Technology Conference, Daytona Beach, 2015.
- [7] G. Strickert, L. Witte, Analysis of the relative motion in a parafoil-load-system, in: 16th AIAA Aerodynamic Decelerator Systems Technology Conference and Seminar, Boston, 2001.
- [8] C. Gorman, N. Slegers, Evaluation of multibody parafoil dynamics using distributed miniature wireless sensors, *J. Aircr.* 49 (2) (2012) 546–555.
- [9] N. Slegers, E. Scheuermann, M. Costello, K. Bergeron, High fidelity in-flight pressure and inertial canopy sensing, in: 23rd AIAA Aerodynamic Decelerator Systems Technology Conference, Daytona Beach, 2015.
- [10] S. Burdette, M. Costello, E. Scheuermann, Using an array of in-canopy sensors for guided airdrop system state estimation, in: 24th AIAA Aerodynamic Decelerator Systems Technology Conference, Denver, 2017.
- [11] N. Carlson, Federated square root filter for decentralized parallel processes, *IEEE Trans. Aerosp. Electron. Syst.* 26 (3) (1990) 517–525.
- [12] D.B. Kingston, R.W. Beard, Real-time attitude and position estimation for small UAVs using low-cost sensors, in: AIAA 3rd “Unmanned Unlimited” Technical Conference, Chicago, 2004.
- [13] A. Chulliat, S. Macmillan, P. Alken, C. Beggan, M. Nair, B. Hamilton, A. Woods, V. Ridley, S. Maus, A. Thomson, The US/UK World Magnetic Model for 2015–2020, NOAA National Geophysical Data Center, Boulder, 2014.
- [14] M.B. Ward, M.R. Cacan, E. Scheuermann, M. Costello, K. Bergeron, G. Noetscher, M. Shurtliff, Flight test results of recent advances in precision airdrop guidance, navigation, and control logic, in: 23rd AIAA Aerodynamic Decelerator Systems Technology Conference, Daytona Beach, 2015.
- [15] M. Ward, Adaptive Glide Slope Control for Parafoil and Payload Aircraft, Ph.D. dissertation, Georgia Institute of Technology, Atlanta, GA, 2012.
- [16] N. Slegers, E. Beyer, M. Costello, Use of variable incidence angle for glide slope control of autonomous parafoils, in: Aerodynamic Decelerator Conference, Williamsburg, VA, 2008.
- [17] M.W.M.C.M.C.E. Scheuermann, Combined lateral and longitudinal control of parafoils using upper-surface canopy spoilers, *J. Guid. Control Dyn.* 38 (11) (2015) 2122–2131.
- [18] Military Specification MIL-F-8785C, 1980.